Research Square

Preprints are preliminary reports that have not undergone peer review.
They should not be considered conclusive, used to inform clinical practice,
or referenced by the media as validated information.

ZC Potentiostat: A Portable, Low-Cost, Edge-AI-Enabled Electrochemical Analyzer for Rapid Lead Screening in Glazed Pottery Foodware

Yomnah A. Hassan
Zewail City of Science and Technology
Omar Ramadan
Zewail City of Science and Technology
Rabeay Y. A. Hassan
Zewail City of Science and Technology
Ahmed S. Abd-Rabou
ahmed.abdrabou@zewailcity.edu.eg
Zewail City of Science and Technology

Research Article

Keywords: Cyclic Voltammetry, Chronoamperometry, Anodic Stripping, Linear Sweep Voltammetry, Machine Learning, PWA, Lead, Glazed Pottery.

Posted Date: November 24th, 2026

DOI: https://doi.org/10.21203/rs.3.rs-11494188/v1

License: This work is licensed under a Creative Commons Attribution 4.0 International License.
Read Full License

Additional Declarations: No competing interests reported.

ZC Potentiostat: A Portable, Low-Cost, Edge-AI-Enabled Electrochemical Analyzer for Rapid Lead Screening in Glazed Pottery Foodware

Yomnah A. Hassan[1,2], Omar Ramadan[3], Rabeay Y. A. Hassan[3], Ahmed S. Abd-Rabou[1,2*]

1 Nanotechnology and Nanoelectronics Engineering Program, University of Science and Technology, Zewail City,12578, Giza, Egypt.

2 Center for Nanotechnology (CNT), University of Science and Technology, Zewail City, 12578, Giza, Egypt.

3 Biosensors Research Lab, University of Science and Technology, Zewail City, 12578, Giza, Egypt.

* Correspondence: E-mail: ahmed.abdrabou@zewailcity.edu.eg (A.S.A.R.)

Abstract

Chemistry, materials science, and biomedical sciences have been interested in potentiostats to determine various parameters in electrochemical experiments. This study aimed to implement a portable, low-cost, multi-channel electrochemical analyzer integrated with an on-device machine-learning classifier that gives a binary verdict in real time, displayed in its progressive web application. Scans are stored in a cloud database, from which the training data were exported; the model can be retrained as more scans are collected. Its operating techniques are cyclic voltammetry, linear sweep voltammetry with an anodic stripping option, and chronoamperometry in a potential range of ±1.5 V for three different current ranges from ±50 µA to ±1.5 mA, with one channel assigned for each current range. The analyzer costs only $43. It was validated on a redox reaction using the ferricyanide couple, then on our main application: an anodic stripping binary classifier for lead leached from glazed pottery foodware. All experiments were conducted against a commercial potentiostat. The lead calibration was linear (R^2 = 0.99) with a limit of detection of 0.79 mg L^{-1} in the leachate against the 4 mg L^{-1} limit for Category 2 ceramic articles. As a proof-of-concept, we conducted 30 leave-one-out cross-validation runs on balanced datasets of 22 scans, and it distinguished safe from unsafe scans with 88.0% ± 2.2% accuracy

against a 50% baseline. Four leachates were analyzed by atomic absorption spectrometry, and the safe/unsafe classification agreed with the commercial instrument's calibrated result and with AAS.

Keywords:

Cyclic Voltammetry, Chronoamperometry, Anodic Stripping, Linear Sweep Voltammetry, Machine Learning, PWA, Lead, Glazed Pottery.

1. Background

Potentiostats are widely used in electrochemical measurements to study material properties and surface interactions [1], in biosensing, battery characterization, and biomedical devices [2]. Electrochemical instrumentation has significantly improved due to the continuous increase in computing power [3]. Authors in [4–13] tried to follow the latest characteristics updates in their potentiostat designs, such as being mobile and embedded with high accuracy, fast response, low cost, minimized power consumption and footprint area [14], a user-friendly interface, and multi-modes of operation. The research gap is the post-measurement decision. In designs [4–13], the instrument stops at streaming a voltammogram to a host computer or smartphone, then the interpretation is done by a well-trained user; the devices are typically single-channel, and none convert the curve into a decision on board. For a tool intended for use away from the laboratory, for example at a market, a checkpoint, a clinic, or a classroom, the interpretation step is a remaining barrier. TinyML is used to allow trained neural-network inference to run within the kilobyte-scale memory of our ESP32 microcontroller [15, 16]. Machine learning is increasingly used to extract analytical information from voltammetric data [17]; therefore, combining acquisition and inference on the same device is feasible and useful for field screening. The purpose of this study is to implement a full analyzer with a low-cost multi-channel capability, integrated with TinyML and a PWA that can screen safe/unsafe lead leaching from

glazed pottery foodware as a demonstration of an application with immediate public health relevance. It is designed for the three-electrode system and can operate in electrochemical techniques like Cyclic Voltammetry (CV), Linear Sweep Voltammetry (LSV), Anodic Stripping Voltammetry (ASV), and Chronoamperometry (CA) with three different current ranges from ±50 μA to ±1500 μA in three channels, acquired within a single sweep and sent in real time to the web application. The data were stored in the Firebase database and then used for training the model. Acetic foods and drinks can be exposed to lead leached from glazed ceramic foodware [18, 19]. Lead is a cumulative toxicant; a global modeling analysis estimated that in 2019 lead exposure cost children under five 765 million intelligence quotient points, approximately 95% of that loss occurring in low- and middle-income countries [20], precisely the settings in which artisanal glazed ware is produced and used. Lead exposure not only affects the brain but also other organs like the kidney and liver [18]. Young children absorb 4–5 times as much ingested lead as adults [18]. In developing countries, child labor is common, especially in workshops like those of artisans, so those children will not only be exposed to lead from acidic food in poorly glazed pottery but also during their work through dust inhalation that contains lead [18]. In 2023, the Institute for Health Metrics and Evaluation (IHME), reported that lead exposure caused approximately 3.5 million deaths globally due to cardiovascular effects and about 71.5 million years lost to disability [18]. The lead concentration is usually verified by confirmatory methods that require a well-equipped laboratory with Atomic Absorption Spectrometry (AAS) or Inductively Coupled Plasma Mass Spectrometry (ICP-MS) [21, 22], which require a well-trained user, and this is not accessible at the point of need, like artisans, vendors, and inspectors; moreover, the cost of such a test is high, and the process takes much time. A device that can measure the released lead in less than 5 minutes and yet make

a decision on whether the safety limit is exceeded will make it much easier for non-specialists to use it at their point of need. Migration of lead from ceramic articles is subject to safety restrictions by the European Union (EU) and United States (US) release limits; the EU has a limit of 4.0 mg L^{-1} for Category 2 fillable hollow-ware under a standardized 4% acetic acid extraction[21, 23], with test procedures defined in ISO 6486 and ASTM C738 [22, 23], while the US applies a stricter 0.5 mg L^{-1} action level for cups and mugs [24]. The articles examined here are Category 2 fillable vessels with internal depths exceeding 25 mm, used to hold food. Anodic stripping voltammetry pre-concentrates the analyte at the electrode, is well suited to trace lead determination with portable instrumentation [25, 26], and has been demonstrated for lead [27]. The specific problem of lead released from glazed ceramics has itself been addressed electrochemically: bismuth-film-modified screen-printed electrodes (SPE) have been applied to released lead in Moroccan ceramic ware [28], establishing that stripping voltammetry at disposable electrodes is a viable route to this determination in a regional artisanal-pottery context; the present work extends that approach by integrating the measurement and its interpretation on a self-contained instrument.

The full proposed analyzer combines a 24-bit analog-to-digital converter (ADC), three different channels, a three-electrode analog front end, and a bipolar power supply, all controlled by an ESP32 microcontroller. It performs data acquisition, signal processing, and runs a compact on-device machine learning classifier to return a safe/unsafe verdict to the user directly via the PWA. The device was benchmarked against a commercial potentiostat to validate our results in electrochemical characterization by a reversible redox reaction and analytical calibration. Both showed excellent linearity in the calibration (R^2) and matched diffusion-controlled voltammetry. A detailed comparison of the ZC Potentiostat specifications against representative

low-cost designs is deferred to Section 3.3; it has the specification gaps in prior work and how the present design addresses them.

2. Materials and Methods

2.1. Device top-level design

The first block of the design is the input stage; it consists of a 12-bit Digital-to-Analog Converter (DAC) that is controlled by the microcontroller (ESP32-WROOM module), three control amplifiers, and three current-sensing converters for the three channels. It works as follows: the control amplifier feeds the electrochemical cell (EC) with the applied potential generated from the DAC. The current-sensing converter converts the cell's resulting current to a voltage across its corresponding channel. The second block is the output stage, which consists of a 24-bit Analog-to-Digital (ADC) converter that digitizes the EC's current response and sends it to the microcontroller. Each scan has two modes of processing: plain mode and classification mode. Each anodic-stripping scan is classified on board by the microcontroller; the scan and its verdict are then sent to the Firebase cloud database (the PWA's back end), where they are stored and displayed in the PWA in either plain mode (no verdict) or classification mode. Fig. 1 shows a system block diagram, and Fig. 2 shows the assembled instrument in operation: the three-electrode cell, the analyzer, and the web application on a laptop. Table 1 summarizes the full hardware and firmware specifications for the device.

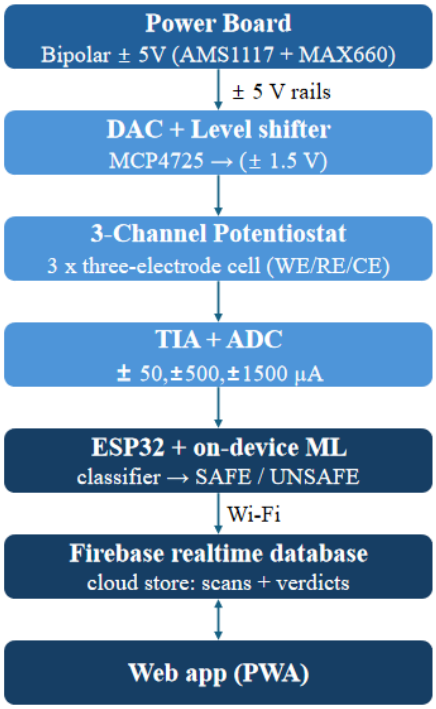


Fig. 1 System block diagram.



Fig. 2 The assembled instrument in operation.

Table 1 ZC Potentiostat hardware and firmware specifications.

Parameter	**Specification**
Microcontroller	ESP32-WROOM.
ADC	ADS1220, 24-bit delta-sigma.
DAC	MCP4725, 12-bit.

Potential range	−1.5 to +1.5 V.
Samples per scan	Up to 1024 (fixed acquisition buffer).
Potential step	DAC-limited resolution ≈ 0.8 mV (12-bit MCP4725, 3.3 V reference). A fixed 1024-point acquisition buffer limits the number of points per scan, setting the minimum step to about 6 mV for a full ±1.5 V cyclic sweep, and proportionally finer for narrower windows.
Scan-rate range	10 to 150 mV s^{-1}.
Current ranges (3 channels, acquired within a single sweep)	±50, ±500, ±1500 µA.
Techniques	CV, CA, LSV, ASV.
On-device analysis	Embedded multilayer-perceptron classifier (289 parameters).
Interface	Wi-Fi; Firebase cloud backend; PWA.
Power	± 5V (AMS1117 + MAX660).
Operational amplifiers	LM324N.

Approximate unit cost	USD 43

2.2. Analog Front-End Design

The analog front-end circuitry was adapted and modified from that of Anshori et al. [14]. However, the proposed device digitizes the current with an external 24-bit ADC (ADS1220). Furthermore, it supports a current range of ±50 μA to ±1.5 mA across three distinct channels, offering a broader operating range than that reported by Anshori et al. [14]. Finally, integration with PWA, along with on-device machine learning and IoT enables real-time data monitoring, control, and classification, which provides an additional advantage of the proposed design.

The first block is the control block. It starts with the microcontroller, with the firmware ordering the start of the process, the step size, the operational mode, the scan rate, the start and end voltage values, and the selected channel. ESP32-WROOM microcontroller was selected because it supports wireless connectivity via its built-in Wi-Fi module. It also has sufficient memory for the on-device classifier. It has already also been demonstrated in other comparable low-cost potentiostat designs in the literature [9, 14] and is locally available in the market.

The second stage is a DAC that converts the digital signal from the microcontroller to an analog signal for the electrochemical cell. MCP4725 12-bit DAC IC was selected; it is already demonstrated in other potentiostat designs in the literature [14, 29]. It gives an expected input resolution of up to 0.81 mV (3.3 V reference). Then, a level-shift amplifier is designed to convert the unipolar signal to a bipolar signal to feed the electrochemical cell. This signal is required to be strong, with high input impedance and low output impedance. So, a voltage follower or buffer is added before the level shifter. The three channels form three independent potentiostat loops: in each, an LM324N control amplifier drives that channel’s counter electrode. Hence, in every channel, the working-to-reference potential follows the same DAC command.

The second block is the data acquisition block. The output block starts with a current-sensing/level-shifting inverting amplifier circuit (LM324N) to convert the electrochemical cell output current into a voltage within the working unipolar range.

The expected ranges are -50 µA to 50 µA in the first channel, -500 µA to 500 µA in the second channel, and -1.5 mA to 1.5 mA in the third channel. The next step is to convert this analog signal back to digital using the ADS1220 24-bit ADC, which the microcontroller reads in the final stage of this block. It has a sigma-delta ADC configuration to take advantage of the anti-aliasing filter to reduce the noise for better performance.

The microcontroller includes an embedded ADC module. However, an external ADC integrated circuit (IC) is used instead because the microcontroller is limited by the number of bits, and the required resolution exceeds that limit. Another reason for using the external ADC module is its greater reliability with analog signals than the microcontroller's ADC. It has four input channels; three of them are used for the three channels, and the fourth input is connected to the level-shifter output and read at each potential step, providing a direct measurement of the applied working-electrode potential; this measured potential is used as the potential axis of all scans. We plan to use this input as a fourth channel in future work by deriving the potential from a calibrated DAC output **(**Section 3.6). The next stage is a buffer and a voltage regulator using Zener diodes (BZX79-C3V3) to protect the next stage from unexpected voltage values from the electrochemical reaction, which could damage the system.

The op-amp IC used for all amplifier positions is the LM324N. It is a general-purpose op-amp. It was chosen for its local availability, and its common-mode input and output ranges were verified in similar low-cost designs [14] to suit the ±5 V rails, low-frequency, modest-current voltammetric signals, and the resolution targeted in this

work. Future work will involve a precision low-noise amplifier to lower the noise floor, as stated in Section 3.6.

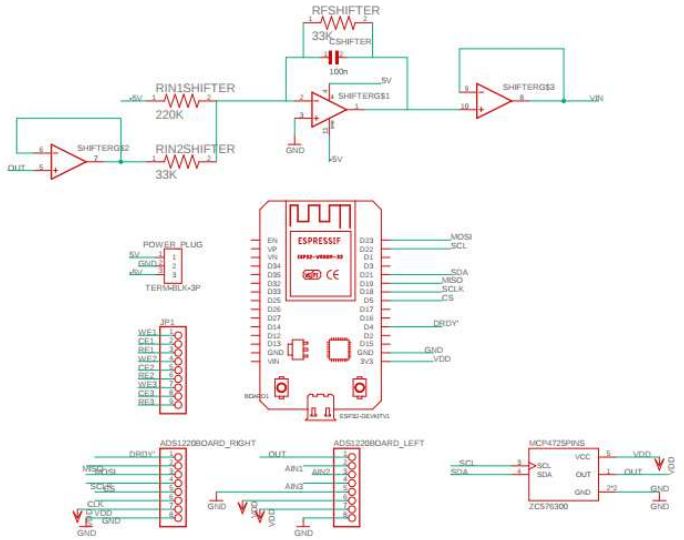


Fig. 3 a

Analog front-end schematic part (a): a microcontroller, a level shifter, an ADC module, a DAC module pin header, a power plug pin header, and nine electrode pin headers.

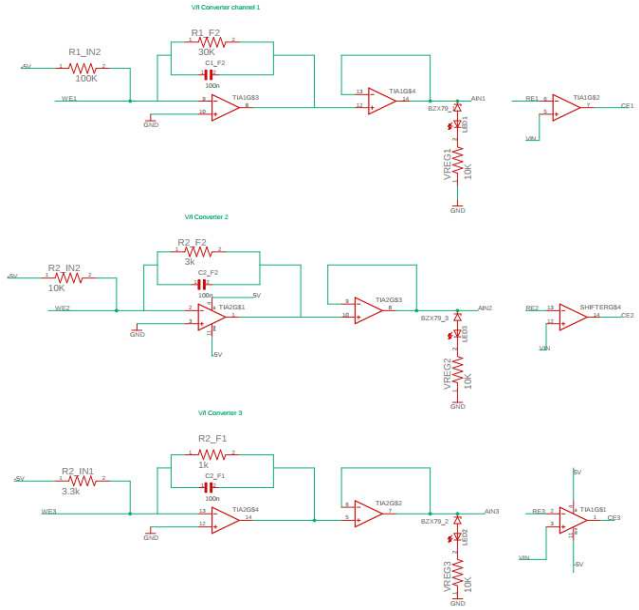


Fig. 3 b

Analog front-end schematic part (b): three-stage current-sensing/level-shifting inverting amplifier circuits, voltage regulators, buffers, and control amplifiers.

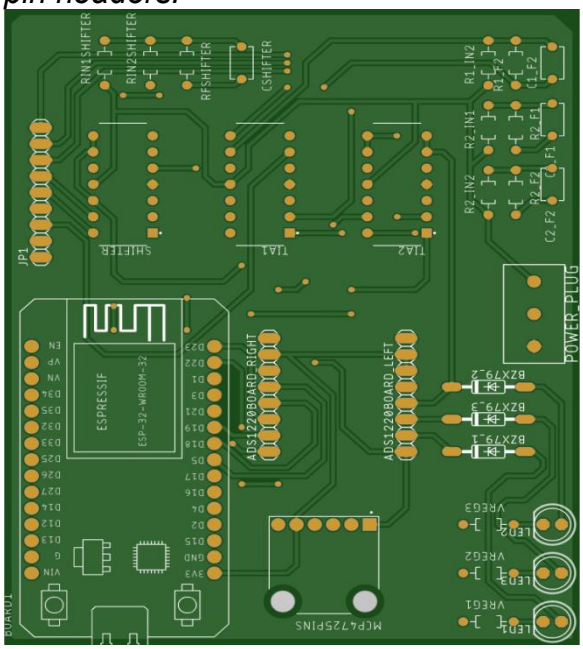


Fig. 4 a

Analog front-end PCB top layer

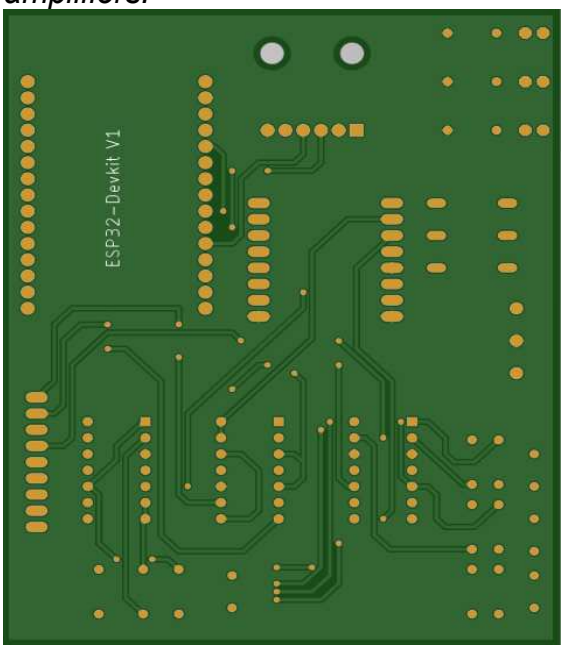


Fig. 4 b

Analog front-end PCB bottom layer

2.3 Power Supply Circuitry

A dedicated power supply circuitry was designed to feed the required bipolar ±5 V supply, with a low-dropout regulator (AMS1117-5) for the +5 V rail and a switched-capacitor voltage inverter (MAX660), which transfers charge through a flying capacitor, to generate −5 V. A 6 V rechargeable battery was used as the main input for this circuitry, while the ESP32 is powered over USB. The positive and negative rails supply power only to the LM324N op-amps, while the microcontroller supplies the 3.3 V for digital ICs. Each rail uses a Pi-type (C–L–C) filter to attenuate the charge pump's switching ripple before it reaches the measurement circuitry. A power-on LED (LED1) with a 1 kΩ series resistor (R1) on the +5 V rail indicates if the board is powered, and the regulated ±5 V rails and ground reach the front-end board (POWER_PLUG) through the three-terminal plug (U3). Figs. 5, 6a, and 6 b show the power schematic and layout for the top and bottom layers, respectively.

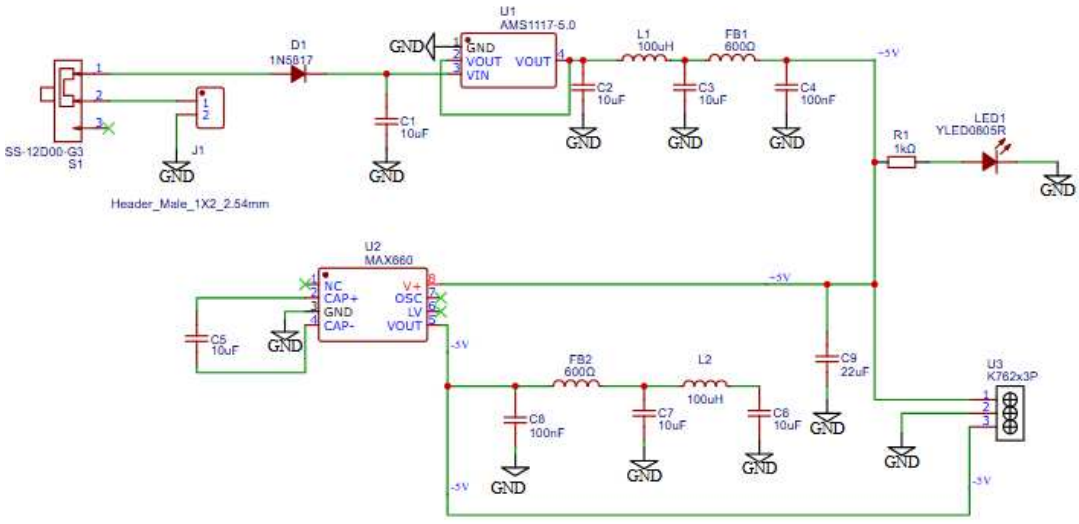


Fig. 5 Power circuitry schematic

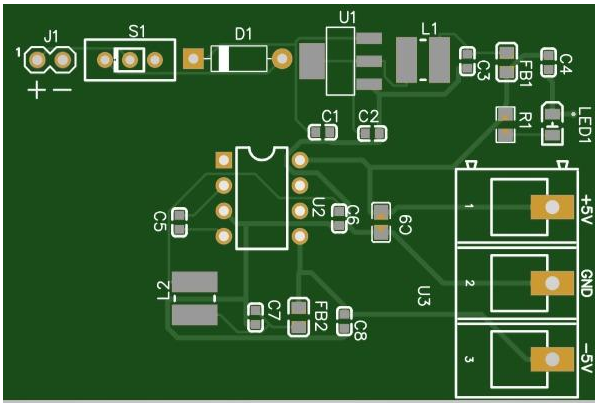


Fig. 6 a
Power circuit PCB top layer

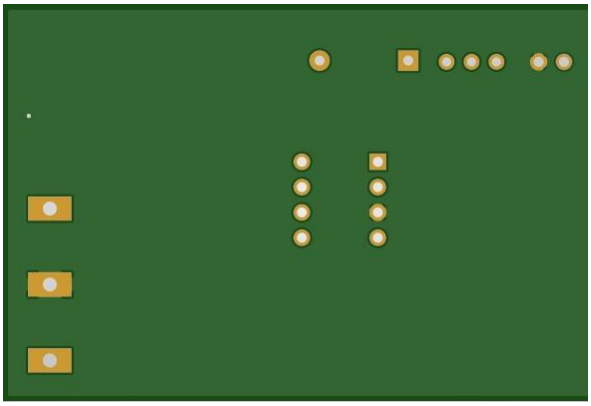


Fig. 6 b
Power circuit PCB bottom layer

2.4. Printed Circuit Board Design and Fabrication

The PCB design was conducted using Eagle Autodesk 9.5.2 free software with double-layer capabilities. The system is divided into two PCBs: the analog front-end board and the power supply board, so that each stage can be evaluated and debugged separately. Integrating both PCBs into one board is considered in future work, as stated in Section 3.6. The analog front-end PCB measures 80 mm × 100 mm, and the power board measures about 60 × 40 mm. Both PCB layouts are dual-sided boards with a continuous ground plane across the entire area; this layer separation helps minimize crosstalk and interference between signals, improving overall performance. They consist of surface-mount and through-hole components. The surface-mounted components are integrated as breakout boards, such as the MCP4725 and ADS1220 boards, because these are the available forms of these ICs from local vendors.

2.5. Firmware

The firmware was compiled and uploaded to the ESP32 via Arduino IDE. The time it takes to send data to the cloud database over Wi-Fi may disturb the measurement timing, so the complete scan is buffered locally and transmitted to the cloud backend only after acquisition finishes. The scan works as follows: the user enters the specific potential profile via the scan window in the PWA, then the DAC is adjusted to output the desired voltage and waits for the signal to settle, then reads the resulting current from the ADC and saves the (potential, current) pair as a data point. This process is repeated across the whole voltage range the user set. After the scan is completed, eight specific curve features are calculated, and the classifier is run. The user can optionally do the following for the displayed curves: de-spiking with a three-point median filter, showing the peak current above a local baseline set by the user, getting the delta I value over a specific shoulder for the baseline, and smoothing the curve. All these options are for display; the raw data are stored in Firebase database.

2.6. Machine Learning Interface

After each anodic-stripping scan, the firmware extracts eight features from the three-point median-filtered current: ΔI, E at I_peak, peak area, and half-height width within the −0.50 to −0.28 V baseline window; baseline slope and level; and the current range and standard deviation over the whole sweep. Scans with accepted peaks are then standardized and passed to a compact multilayer perceptron (8 → 16 → 8 → 1); scans without an accepted peak are reported as safe. The platform thus follows the TinyML paradigm of on-microcontroller inference [15, 16]. The off-device training was done from the recorded feature set, and the resulting weights were exported to the firmware and the PWA. The memory footprint is negligible, and the verdict is produced in situ on the microcontroller without host-side computation; this on-device execution of the classifier distinguishes the platform from prior low-cost designs compared in Table 4. The classifier was trained on a set of scans (n = 22, balanced classes) as a proof-of-concept to demonstrate the full

pipeline. The collection of a larger data set for a definitively trained and validated classifier is identified as future work in Section 3.6.

2.7. Cloud database and PWA

The device requires a Wi-Fi connection: it receives scan requests from and writes scans and verdicts to the Firebase database. This cloud database stores all the datasets used to train the model. The user can select between two modes: plain mode and classifier mode. Plain mode shows only the voltammograms without verdicts, while classifier mode offers selectable verdicts (safe/unsafe, positive/negative, below/above, pass/fail). Earlier scans and their verdicts can be reloaded from the cloud database and exported as CSV without connecting the instrument. Figs. 7(a-d) show the PWA voltammograms with the color-coded safe/unsafe banner and the add scan window, which prevents the user from entering out-of-range values. It also rejects scan-rate/step combinations that would require a per-step period below the device's 90 ms minimum (set by the multi-channel acquisition time), so infeasible fast scans are never dispatched.

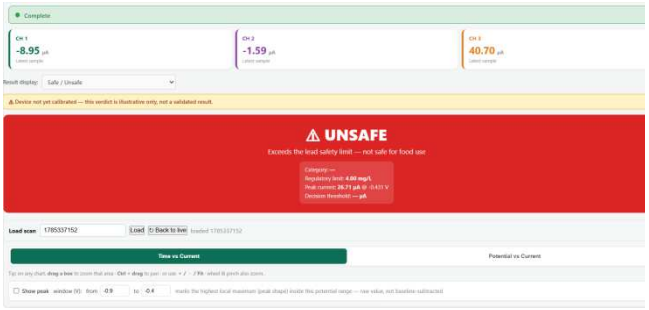


Fig. 7a

PWA snippet (a) showing a screening result



Fig. 7b

PWA snippet (b) showing the table and an ASV on channel 3

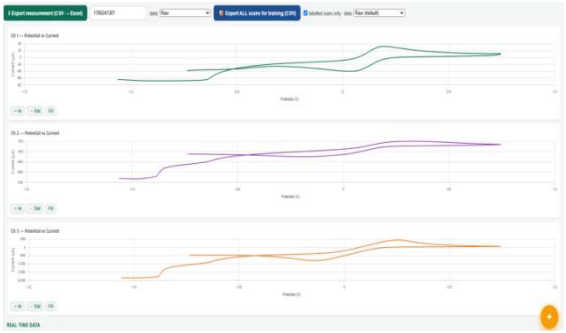


Fig. 7c

PWA snippet (c) showing the voltammograms of the three measured channels.

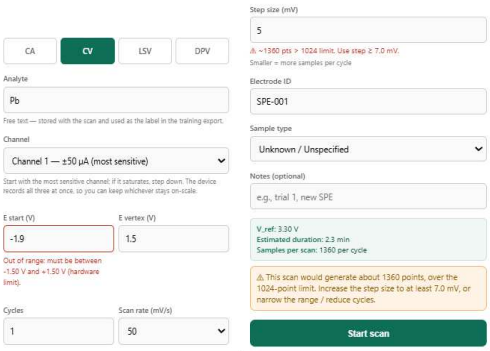


Fig. 7d

PWA snippet (d) showing the add scan windows while preventing the user from adding any out-of-range values.

2.8. Electrochemical Validation Methodology

The instrument was validated as follows.

(i) The diffusion-controlled behavior was tested following the Randles–Ševčík equation (1) by CV scans on the reversible $[Fe(CN)_6]^{3-/4-}$ couple in 0.1 M KCl electrolyte at different scan rates of 10 to 100 mV s^{-1} with a 10 mV potential step [30].

$$I_p=(2.69\times10^5)\, n^{\frac{3}{2}}\, A\, C\sqrt{(D\, v)} \qquad (1)$$

(ii) The three-range channels were demonstrated by connecting three independent cells, containing 15, 45, and 150 mM ferricyanide, to the ±50, ±500, and ±1500 µA channels, respectively, and acquiring all three in a single cyclic voltammetric run.

(iii) Linear-sweep voltammetry and chronoamperometry were recorded on the same couple to demonstrate the remaining two techniques.

(iv) The device was calibrated for Pb^{2+} over nominal concentrations of 2–10 mg L^{-1} in 0.1 M HNO_3. All lead experiments were conducted using the ASV technique with a potential window from -0.7 to -0.1 V, a scan rate of 50 mV s^{-1} and the deposition potential was set to -0.7 V for 120 seconds. Limits of detection and quantification were derived from seven

replicate blank measurements of the supporting electrolyte (0.1 M HNO_3), and standards falling below the detection limit were excluded from the regression.

(v) Instrument repeatability was computed by a triplicate scan of a lead standard (4 mg L^{-1}) in 0.1 M HNO_3, and it gave an RSD of 2.6%.

(vi) The same standards, samples, ferricyanide CV, LSV, ASV, and CA were measured on a commercial research-grade potentiostat (PalmSens) and processed with the same peak-extraction method, for an inter-instrument comparison. Appendix A explains any parameter differences.

(vii) Matrix accuracy was assessed by a spike recovery in a real glazed-pottery leachate: an unspiked leachate and the same leachate spiked with a known amount of Pb^{2+} were measured on the same conditioned electrode surface, and the recovered amount was compared with the amount added.

(viii) Cd(II), Zn(II), and Ni(II) were assessed in a 0.1 M HNO_3 electrolyte at a 1:1 mass ratio, and the lead-stripping peak was measured against a lead peak on the same CPE surface for each metal individually.

The electrode configuration differed by experiment; for the ferricyanide measurements, the working electrode was the working electrode of an SPE (Zensor), and two silver wires were used for the counter and pseudo-reference electrodes. For the lead measurements, two carbon-paste electrodes were used as working and counter electrodes with an Ag/AgCl reference electrode. Deaeration was omitted as a deliberate simplification for field use. Full procedures (leachate preparation, deposition parameters, baseline window) are provided in Section 3.2 and Appendix A.

3. Results and Discussion

3.1. Electrochemical Performance and Technique Demonstration

In the CV experiment of the ferricyanide couple, a 5 mM ferricyanide cell was evaluated by both devices using a 10 mV step size and a potential window of ±0.75 V at different scan rates from 10 to 100 mV s^{-1}. Anodic peak currents for both devices behaved linearly with the square root of scan rate according to equation (1), ZC Potentiostat: $I_{pa} = 4.44 \cdot \sqrt{v} + 3.24$ µA ($R^2 = 0.998$), while the commercial potentiostat: $I_{pa} = 4.18 \cdot \sqrt{v} - 1.30$ µA ($R^2 = 0.997$). The two instruments produce cyclic voltammograms with the same shape and scan-rate dependence, but their peak currents differ, as shown in Fig. 8c, because both devices were run in separate sessions; the linearity agreed closely between the two instruments, as shown in Fig. 8d. The residual slope difference is attributed to electrode area and session-to-session variability rather than to the instrument. This confirms a diffusion-controlled response for the proposed device and proper potentiostatic operation, as indicated by the excellent R^2 value. The 150 mV s^{-1} scan is reported separately to illustrate the maximum scan rate capability of the device, with a step size of 15 mV to maintain an adequate number of points per sweep; the voltammogram is shown in Appendix A. Fig. 8 (a- d) shows CV voltammograms with 5 mM potassium ferricyanide at different scan rates for: a) the proposed device. b) The commercial device. c) Overlapping plots for both devices. d) Linearity plot for both devices.

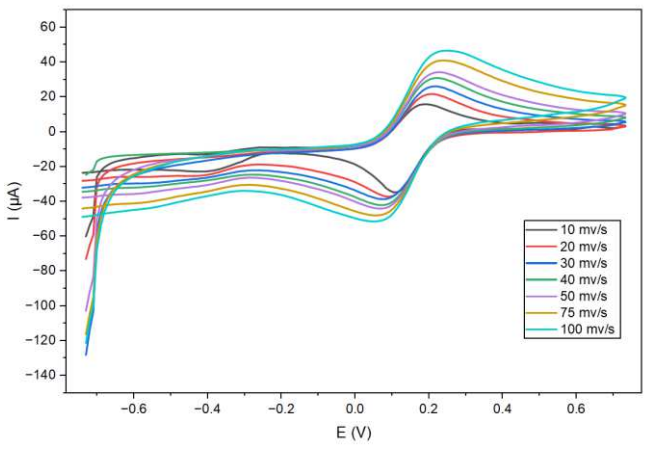


Fig. 8a

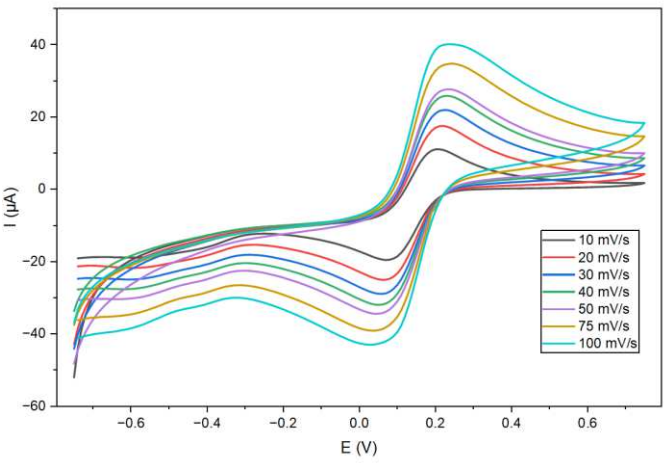


Fig. 8b

ZC potentiostat CV voltammograms at different scan rates.

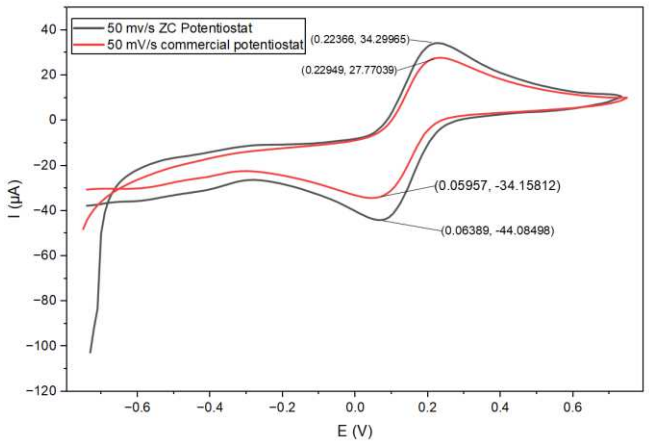
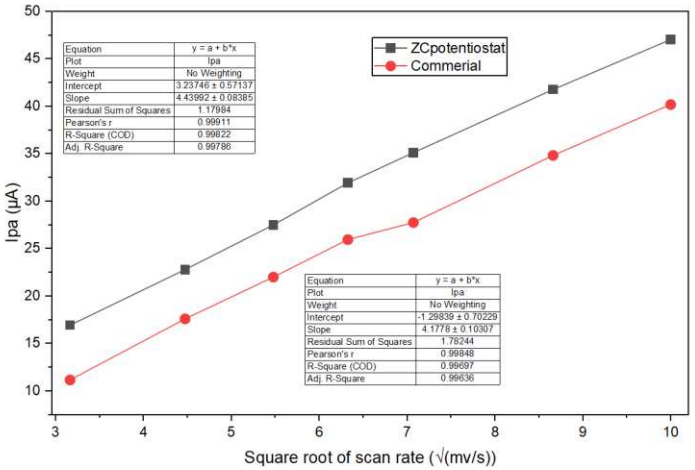


Fig. 8c

Overlapping plots for both devices.

Commercial CV voltammograms at different scan rates.



Equation	y = a + b*x
Plot	Ipa
Weight	No Weighting
Intercept	3.23746 ± 0.57137
Slope	4.43992 ± 0.08385
Residual Sum of Squares	1.17984
Pearson's r	0.99911
R-Square (COD)	0.99822
Adj. R-Square	0.99786

Equation	y = a + b*x
Plot	Ipa
Weight	No Weighting
Intercept	-1.29839 ± 0.70229
Slope	4.1778 ± 0.10307
Residual Sum of Squares	1.78244
Pearson's r	0.99848
R-Square (COD)	0.99697
Adj. R-Square	0.99636

Fig. 8d

Linearity plot for both devices.

307 In the three-channel run described in Section 2.8 (ii), anodic peak currents of 32.5, 97.9 and
308 443.7 µA were recorded on the ±50, ±500 and ±1500 µA channels, respectively, showing
309 that the three TIA stages are all read at every potential step, each within its own range, in a
310 single acquisition. Figs. 9 (a- c) show the three-channel voltammograms.

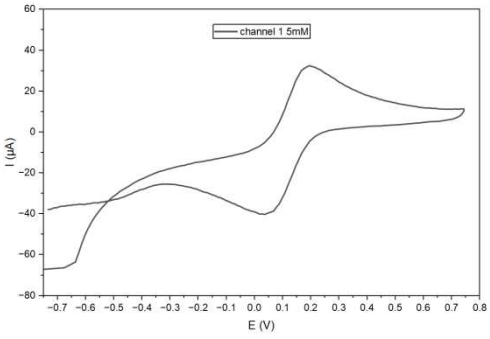


Fig. 9a

Channel 1

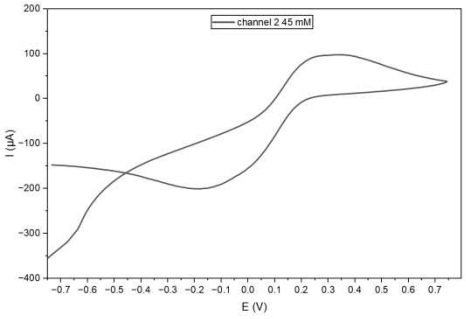


Fig. 9b

Channel 2

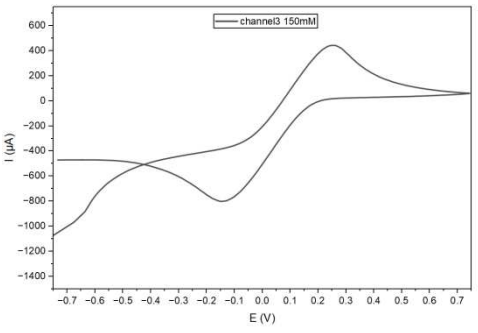


Fig. 9c

Channel 3

311 Linear-sweep voltammetry on the same couple was demonstrated in its plain, non-stripping
312 form. It produced the expected wave against the silver pseudo-reference electrode. The two

overlapping curves in Fig. 10a are nearly coincident, with the same peak potential and nearly the same peak current.

Chronoamperograms confirmed the Cottrell behavior equation (2); the current was fitted to $1/\sqrt{t}$ for both instruments from t=1 to 5 s, after the initial charging transient had decayed, giving R^2 values of 0.9999 and 0.9991 for the ZC Potentiostat and the commercial one, respectively as shown in Fig. 10c. The difference in current values shown in Fig. 10b is because the commercial device reports the first settled point; however, the proposed device samples the E step without front-end settling.

$$I(t)=\frac{nFA\sqrt{DC}}{\sqrt{\pi}\cdot\sqrt{t}} \qquad (2)$$

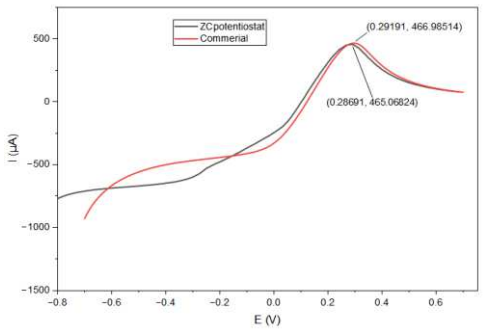


Fig. 10a

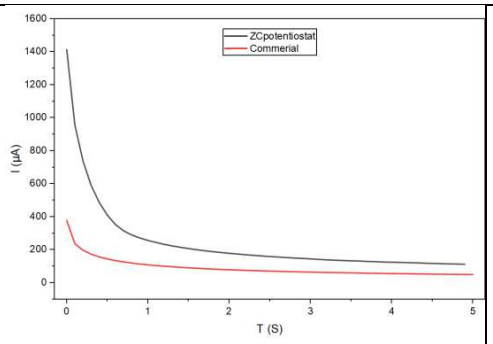


Fig. 10b

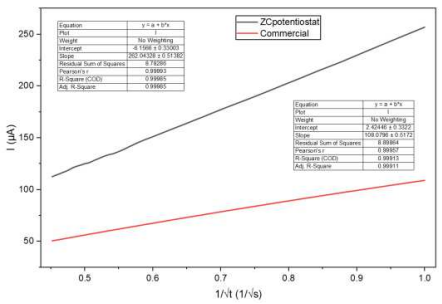


Fig. 10c

Overlapping LSV for both devices.	Overlapping CA for both devices.	Cottrell behavior curves for both devices.

3.2. Rapid Lead Screening in Glazed Pottery Application

To demonstrate the instrument on a problem with social consequences, glazed pottery foodware was randomly collected from local markets in Egypt for released lead screening. The calibration curve for Pb^{2+} was obtained using ASV across the nominal range of 2–10 mg L^{-1} for both instruments. Our device gave a linear response of $I_p = 4.03 \cdot C + 4.45$ µA (R^2

= 0.992) while the commercial one had I_p = 3.12·C + 2.54 µA (R^2 = 0.989). The residual difference between the two is attributed mainly to electrode-surface and session variability, as well as a difference in the potential step (5 mV in the ZC potentiostat vs. 10 mV in the commercial one). At the 6.67 mg L^{-1} cell-frame decision boundary (4.0 mg L^{-1} in the leachate), both instruments respond linearly, so the difference in sensitivity does not affect the classification task. Figs. 11(a–c) show the ZC Potentiostat and commercial calibration voltammograms and the combined linearity plot. For Limit of Detection (LOD) and Limit of Quantitation (LOQ) calculations, we obtained seven scans in blank measurements in 0.1 M HNO_3 with a mean of 3.93 µA and a standard deviation of 1.60 µA. Following ICH Q2(R2) convention [31], equations (3) and (4), with the calibration slope S = 4.03 µA L mg^{-1}, give LOD= 1.31 and LOQ= 3.97 mg L^{-1}, corresponding to 0.79 and 2.38 mg L^{-1} in the leachate.

$$LOD = \frac{3.3 \times \sigma}{S} \qquad (3)$$

$$LOQ = \frac{10 \times \sigma}{S} \qquad (4)$$

Repeatability from three consecutive anodic-stripping scans of a 4 mg L^{-1} Pb^{2+} standard, recorded on the same conditioned electrode surface, gave a relative standard deviation of 2.6% (n = 3). Standards at 0.5 and 1.0 mg L^{-1} were also measured by both devices but yielded stripping peaks below the mean blank response and differed by less than the blank standard deviation; so, they were excluded from the calibration. However, their voltammograms still appear in Fig. 11a and b (calibration curves) for illustration.

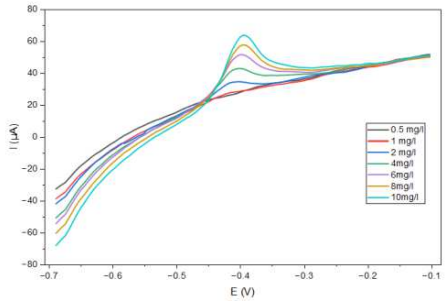
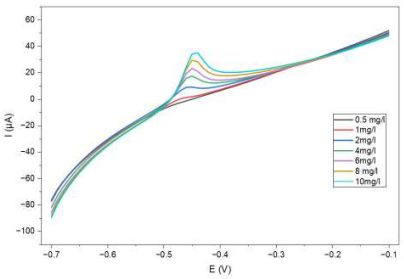
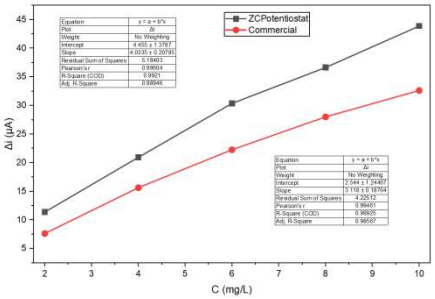
 Fig. 11a	 Fig. 11b	 Fig. 11c
ZC potentiostat standard calibration ASV.	Commercial potentiostat standard calibration ASV.	Linearity plot for both devices.

Table 2 summarizes key figures of merit for this experiment.

Table 2*. Analytical figures. of merit for rapid lead screening experiments using the ZC Potentiostat (Pb²⁺, anodic-stripping linear-sweep voltammetry).*

Parameter	**Value**
Calibration equation	I_p = 4.03·C + 4.45 μA
Linear range	2–10 mg L^{-1}
Coefficient of determination (R^2)	0.992
Blank response, mean ± SD	3.93 ± 1.60 μA (n = 7)
Limit of detection (cell)	1.31 mg L^{-1}
Limit of quantification (cell)	3.97 mg L^{-1}
LOD / LOQ (leachate)	0.79 / 2.38 mg L^{-1}
Repeatability (RSD, n = 3)	2.6%

The proposed device's detection limit in leachate (0.79 mg L^{-1}) is much higher than that reported for modified-electrode approaches like Mandil and Amine [28] which achieved a detection limit of 4 μg L^{-1} for lead in ceramic leachates using bismuth-film-modified SPE with

square-wave stripping detection. However, we don't aim to advance analytical sensitivity; the main contribution of this work is integrating acquisition, connectivity, and on-device interpretation into a single low-cost instrument.

Accuracy in the sample matrix was assessed by spike recovery in a real glazed-pottery leachate. L7 was measured unspiked and again after addition of 1.98 mg L^{-1} Pb^{2+}. Applying the calibration slope S in equation (5):

$$C_{measured} = \frac{I_{spiked} - I_{unspiked}}{S} \quad (5)$$

yields a $C_{measured} = 2.10\ mg\ L^{-1}$ which gives a spike recovery of 106.1% following equation (6):

$$Recovery = \frac{C_{measured}}{C_{added}} \times 100 \quad (6)$$

Potential interference from divalent metals that may be co-extracted from ceramic glazes [32, 33] was evaluated in 0.1 M HNO_3 at a 1:1 interference-to-lead mass ratio, with each interferent compared against an immediately preceding lead-only reference measured on the same electrode surface, each in a separate cell. Retention of the lead stripping peak was 110.0% for Cd(II), 104.6% for Ni(II), and 98.0% for Zn(II). Cd(II) increased the lead signal by 10%, at the edge of the usual ±10% tolerance. The lead peak potential was unchanged in all three cases (Cd −0.417, Ni −0.407, Zn −0.397 V in both reference and mixture).

The glazed-pottery leachates were screened against the 4.0 mg L^{-1} action level by applying the calibration in Section 3.2 and converting each cell concentration to leachate concentration (leachate = 0.6 × cell; Appendix A); 7 of the 16 leachates were flagged as unsafe. The on-device classifier returned the same safe/unsafe verdict for all 16 leachates

(Section 3.4). For the commercial instrument, verdicts were obtained in the same way using its own calibration (I_p = 3.12·C + 2.54 µA). The classifier's performance is reported in full in Section 3.4. Four leachates **(**L8, L9, L13 and L14**),** one below and three above the action level, were additionally analyzed by AAS, the reference method prescribed by Council Directive 84/500/EEC [21], and measured on the commercial instrument (PalmSens). All three methods returned the same verdict for every sample, including L14, which AAS placed at 4.8 mg L^{-1}, immediately above the 4.0 mg L^{-1} limit.

Table 3. *Screening verdicts for the four archived leachates by the ZC Potentiostat, the commercial instrument, and confirmatory AAS.*

Sample	**ZC Potentiostat**	**PalmSens**	**AAS**
L8	Safe	Safe	Safe (< LOD)
L9	Unsafe	Unsafe	Unsafe (≫ limit)
L13	Unsafe	Unsafe	Unsafe (≫ limit)
L14	Unsafe	Unsafe	Unsafe (4.8 mg L^{-1})

3.3 A General Comparison with other low-cost potentiostats in the literature

Table 4 shows the Potentiostats' limitations in the literature and how we address them in the proposed device. As shown in Table 4, devices like [9, 10, 12, 14, 34] have small current ranges, which limit their applications and make them unsuitable for broader current range applications. The proposed device addresses this issue by dividing a wider current range into three independent channels. The ADC bits are also limited in [10, 12] and the DAC bits are limited in [9, 35], which also limits the current and the applied-signal precision, respectively. This issue is solved by adding external ADC and DAC with more bits for finer current readings and applied-potential steps. The voltage sweep range is limited in [12, 29, 36]. To address this limitation, a wider voltage range is offered. Higher current ranges or resolutions like [34, 36, 37] cost more, which may limit their adoption in highly resource-

constrained environments. The proposed design aims to balance better resolutions with an affordable price, costing $43 and offering multi-channel capability: three channels, one for each current range. The main limitation of these designs is that each instrument delivers a voltammogram for off-device interpretation by a trained user; none convert the curve into an on-board decision. The ZC Potentiostat is the only one among the designs compared here that runs the classifier on the microcontroller and mirrors the verdict in a zero-install web application, so interpretation no longer depends on an expert operator. By integrating these components with the Firebase cloud database and the PWA, the potentiostat not only facilitates real-time data logging and analysis but also enables instrument control and cloud storage of the scans.

Table 4. *Comparison of the proposed device with other potentiostats in the literature.*

Previous Work from the Literature	Limitation	The Proposed Device
[5, 9-12, 29, 34–36, 38, 39]	Single channel.	Multi-channel: three.
[9, 10, 12, 14, 34]	Current ranges: (±300 µA), (±225 µA), a few µA, (±500 µA), (±180 µA), respectively.	±50 µA to ±1.5 mA.
[10, 12]	ADC bits: 10.	24 bits.
[9, 35]	DAC bits: 8.	12 bits.
[34, 36, 37]	Cost: $61.5, $60, and $410, respectively.	$43.

[12, 29, 36]	Voltage Range: ±1 V, ±1.2 V, and ±1.1 V, respectively.	±1.5 V.

3.4. On-Device Machine-Learning Classification

The on-device classification was tested on a set of 22 scans (11 safe, 11 unsafe): the 16 real leachates plus six prepared standards added to balance the classes, labelled against the 6.67 mg L^{-1} cell-frame boundary (leachates from the calibration, standards from their prepared concentrations). A leave-one-out cross-validation (LOOCV) pass is unstable on few samples; so, it was repeated over thirty independent runs with different random initializations. The pipeline reached a held-out accuracy of 88.0% ± 2.2% (unsafe recall 85.2% ± 4.5%, specificity 90.9%) against a 50% majority-class baseline. Fig. 12 shows the confusion matrix: 9 of 11 unsafe scans and 10 of 11 safe scans were classified correctly.

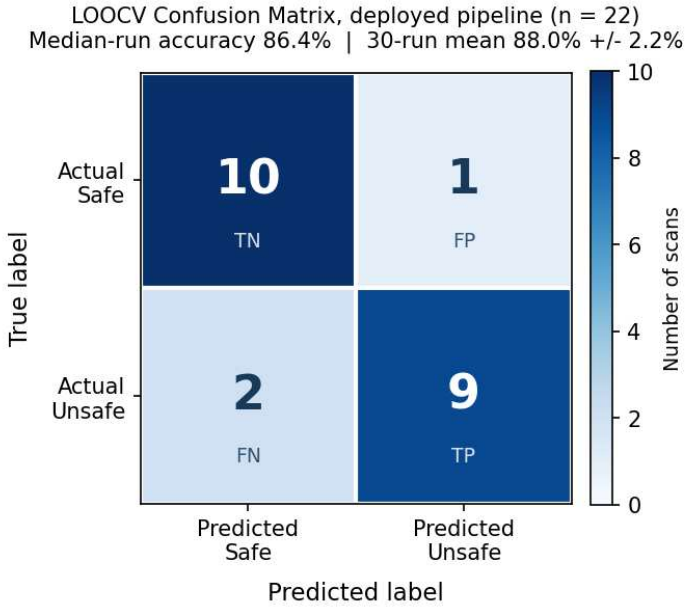


Fig. 12 *LOOCV confusion matrix, one representative run (19/22 = 86.4%); mean over 30 runs 88.0 ± 2.2%.*

Two of the three misclassifications clustered at the decision boundary. Among the prepared standards, the two lying closest to the 6.67 mg L^{-1} cell-frame threshold, 6.37 mg L^{-1} on the safe side and 6.85 mg L^{-1} on the unsafe side, were both misclassified; the third was a 7.82 mg L^{-1} standard predicted safe (misclassified in 19 of the 30 runs); all 16 real leachates

were classified correctly in every run. These results should be read as proof of concept; the dataset limitations and the path to a validated classifier are detailed in Section 3.6.

3.5. Wide-Range Applications

This demonstration illustrates a general capability, as the proposed platform can be extended to other targets. In environmental and food-safety monitoring, anodic stripping determines metals such as cadmium, copper, zinc, mercury, and arsenic, as well as lead, in multiplexed formats [30, 40], enabling the device to be applied to broader heavy-metal screening of water and other foodstuffs.

The multi-channel transimpedance front end, portability, and compatibility with disposable SPE make it suitable for point-of-need and decentralized biosensing, where enzymatic and redox-active analytes are measured amperometrically or voltammetrically [34]. Its low cost and open design make it a practical teaching instrument for electrochemistry and embedded instrumentation [12, 41]. Finally, the embedded-inference approach demonstrated here, which converts a voltammogram into a decision on the device, could be extended to other voltammetric classification tasks given suitable training data, a direction in which machine learning on electrochemical data is moving [17]. Each of these extensions requires target-specific validation and is identified here as a direction rather than a demonstrated result.

3.6. Limitations and Future Work

In future work, we consider using a precise instrumentation op-amp instead of LM324N to lower the noise floor. The analyzer will be modified to have four channels instead of three by deriving the potential axis from a calibrated DAC output, freeing the fourth ADS1220 input for an additional op-amp current stage. We consider integrating the analog front end and the bipolar power supply into one board. The classifier is a proof of concept: it was evaluated on a small dataset, so a larger, class-balanced set of real leachates is considered before its performance can be validated. Samples near the 4.0 mg L^{-1} limit, and screening against stricter limits such as the 0.5 mg L^{-1} US action level, would require confirmation by AAS or

a lower-LOD electrode. Because carbon-paste electrode surfaces are renewed manually, a more stable, reproducible working electrode will be used to improve inter-electrode precision while preserving the platform's low cost and field suitability.

4. Conclusions

A portable multi-channel, low-cost electrochemical analyzer integrated with on-device (TinyML) machine-learning inference and a PWA was proposed and validated over multi-electrochemical techniques: CV, LSV, ASV, and CA. It was benchmarked against a commercial potentiostat (PalmSens) and gave lead calibration linearity of (R^2 = 0.99). We then demonstrated the full process from electrochemical measurement to binary classification for a public-health problem: screening lead in glazed pottery, and its verdict agreed with AAS for all four samples. Compared with the designs in Table 4, the proposed design has several advantages, including multi-channel capability that allows users to run all three channels within a single sweep and supports a wider current range, from ±50 µA to ±1.5 mA. Another advantage is the proposed web app design, which provides data display, instrument control, and cloud storage. However, the main contribution is integrating multi-range acquisition with an on-device verdict. For rapid lead screening, the analyzer reached a detection limit of 0.79 mg L^{-1} in the leachate, a spike recovery of 106% and a repeatability of 2.6% RSD.

Appendix A

The leachates screened in Section 3.2 were obtained from glazed pottery, following ISO 6486-1 and ASTM C738 [22, 23] lead-extraction procedures; a solution of 4% acetic acid was left in each piece of pottery to the brim for 24 hours at room temperature. Then, each 20 mL leachate aliquot was evaporated at 60 °C. Next, we replaced the weak acetic acid with nitric acid to redissolve the residue, using a strong-acid supporting electrolyte suitable for anodic stripping. We also preconcentrated the analyte by a factor of 1.667; the 20 mL

was redissolved in only 12 mL, leachate concentration = 0.6 × cell concentration, and so the 4.0 mg L^{-1} leachate action level corresponds to a decision boundary of 6.67 mg L^{-1} in the measurement cell. Each 12 mL was divided into two cells: one for this device and the other for the commercial one. ASV used a deposition potential of −0.7 V for 120 s, followed by an anodic sweep at 50 mV s^{-1} with a 5 mV step, on carbon-paste working and counter electrodes with an Ag/AgCl reference electrode Section 2.8. The on-device classifier applies its threshold in this cell frame (Section 2.6). It was measured on both instruments with matched acquisition parameters, except that the potential step of the lead calibration series was 5 mV on the ZC Potentiostat and 10 mV on the commercial instrument, while the CV, LSV, and CA comparisons were grid-matched. The step difference was retained because the scan rate was matched (50 mV s^{-1} on both instruments), so only the point density differed, and each calibration was built and evaluated only with standards measured on the same instrument. The PalmSens leachate scans were recorded at a 5 mV step and evaluated with its 10 mV calibration; its concentrations are therefore indicative only, and only its verdicts are reported (Table 3).

Peak heights were extracted from raw Ch3 data without smoothing or despiking; the three-point median filter is applied only within the on-device classifier (Section 2.6) to suppress isolated spikes before feature extraction. A linear local baseline was drawn through the data points nearest −0.50 and −0.28 V, and the lead-stripping peak height (Δi) was taken as the maximum baseline-subtracted current between −0.47 and −0.35 V (peak potential ≈ −0.40 V). The same procedure was applied to all standards, blanks, samples and to the commercial-instrument data.

Fig. 13 shows a separate CV scan for 5 mM potassium ferricyanide on a ZC potentiostat with a scan rate of 150 mV s^{-1}, a step size of 15 mV, and a potential window of ±0.75 V.

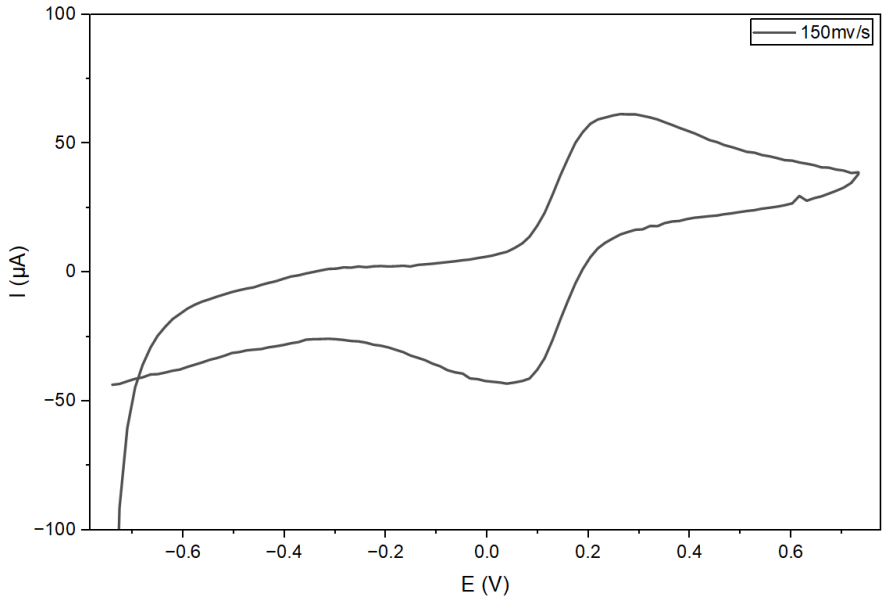


Fig. 13. CV scan for 5 mM potassium ferricyanide on a ZC potentiostat with a scan rate of 150 mV s^{-1}.

Abbreviations

The following abbreviations are used in this manuscript:

Abbreviation	Definition
TinyML	Tiny Machine Learning
US	United States
ICP-MS	Inductively Coupled Plasma Mass Spectrometry
DAC	Digital-to-Analog Converter
CV	Cyclic Voltammetry
CA	Chronoamperometry
LSV	Linear-Sweep Voltammetry
PWA	Progressive Web Application

PCB	Printed Circuit Board
RSD	Relative Standard Deviation
Ag/AgCl	Silver/Silver-Chloride reference electrode
ICH	International Council for Harmonisation
SD	Standard Deviation
ML	Machine Learning
ADC	Analog-to-Digital Converter
TIA	Transimpedance Amplifier
ISO	International Organization for Standardization
AAS	Atomic Absorption Spectrometry
LOD	Limit of Detection
AI	Artificial Intelligence
LOQ	Limit of Quantification
SPE	Screen-Printed Electrode
ASV	Anodic-Stripping Voltammetry
ASTM	American Society for Testing and Materials

EU	European Union
LOOCV	Leave-One-Out Cross-Validation
CPE	Carbon Paste Electrode
EC	Electrochemical Cell
IHME	Institute for Health Metrics and Evaluation
IoT	Internet of things

Declarations

Ethics approval and consent to participate: Not applicable.

Consent for publication: Not applicable.

Availability of data and material: The datasets used and analyzed during the current study are available from the corresponding author on reasonable request.

Competing interests: The authors declare no conflicts of interest. The funders had no role in the design of the study; in the collection, analysis, or interpretation of data; in the writing of the manuscript; or in the decision to publish the results.

Funding: We acknowledge the cost center, IRF ZC 002/2019, from the Research Office at Zewail City, for providing the financial support that enabled us to complete this research.

Authors' contributions:

Yomnah A. Hassan (Y.A.H.): Conducted the main experimental work, developed and implemented the proposed system, performed the experiments, collected and analyzed the data, and prepared the original manuscript.

Omar Ramadan (O.R.): Assisted with chemical preparation, conducted the required laboratory procedures, contributed to the electrochemical experiments, and reviewed the manuscript.

Rabeay Y. A. Hassan (R.Y.A.H.): Provided supervision and expertise in biosensor laboratory procedures, provided laboratory resources, and assisted with experimental design and electrochemical analysis.

Ahmed S. Abd-Rabou (A.S.A.R.): Conceptualized and supervised the overall study, contributed to the analysis of the embedded electronics and TinyML system; reviewed and interpreted the experimental and system-level results, and contributed to the review and revision of the manuscript. He also served as the corresponding author.

Acknowledgments: All experiments were performed in the Zewail City labs, the electronics and biosensors research labs. PCB fabrication was done by Nori Solutions.

Use of generative AI: During this work, the authors used Claude (Anthropic) to assist with manuscript drafting and structuring, developing the progressive web application, writing the model-training notebook, and refactoring the device firmware from a single source file into a modular file structure. All experimental work, sample preparation, measurements, and data collection were conducted by the authors. All datasets and figures presented are derived from real experimental measurements on the physical device. All code was tested and validated by the authors on hardware. No AI tool was used to generate or interpret research data. The authors have reviewed and edited the manuscript in full and take complete responsibility for the content, accuracy, and integrity of this publication.

References

1. Colburn AW, Levey KJ, O'Hare D, Macpherson J V. (2021) Lifting the lid on the potentiostat: a beginner's guide to understanding electrochemical circuitry and practical operation. Physical Chemistry Chemical Physics 23:8100–8117. https://doi.org/10.1039/D1CP00661D
2. Kissinger PT, Heineman WR (eds) (2018) Laboratory Techniques in Electroanalytical Chemistry, Revised and Expanded, 2nd ed. CRC Press
3. Paterson AS, Raja B, Mandadi V, et al (2017) A low-cost smartphone-based platform for highly sensitive point-of-care testing with persistent luminescent phosphors. Lab Chip 17:1051–1059. https://doi.org/10.1039/C6LC01167E
4. Rowe AA, Bonham AJ, White RJ, et al (2011) Cheapstat: An open-source, "do-it-yourself" potentiostat for analytical and educational applications. PLoS One 6:e23783. https://doi.org/10.1371/journal.pone.0023783
5. Arevalo-Ramirez T, Castillo Torres C, Cela Rosero A, Espinoza-Montero P (2016) Low cost Potentiostat: Criteria and considerations for its design and construction. In: 2016 IEEE ANDESCON. Institute of Electrical and Electronics Engineers Inc. https://doi.org/10.1109/ANDESCON.2016.7836211
6. Li YC, Melenbrink EL, Cordonier GJ, et al (2018) An Easily Fabricated Low-Cost Potentiostat Coupled with User-Friendly Software for Introducing Students to Electrochemical Reactions and Electroanalytical Techniques. J Chem Educ 95:1658–1661. https://doi.org/10.1021/acs.jchemed.8b00340
7. Caux M, Achit A, Var K, et al (2022) PassStat, a simple but fast, precise and versatile open source potentiostat. HardwareX 11:e00290. https://doi.org/10.1016/j.ohx.2022.e00290
8. Burgos-Flórez F, Rodríguez A, Cervera E, et al (2022) TBISTAT: An open-source, wireless portable, electrochemical impedance spectroscopy capable potentiostat for the point-of-care detection of S100B in plasma samples. PLoS One 17:e0263738. https://doi.org/10.1371/journal.pone.0263738
9. Anshori I, Mufiddin GF, Ramadhan IF, et al (2022) Design of smartphone-controlled low-cost potentiostat for cyclic voltammetry analysis based on ESP32 microcontroller. Sens Biosensing Res 36:100490. https://doi.org/10.1016/j.sbsr.2022.100490
10. Cordova-Huaman A V., Jauja-Ccana VR, La Rosa-Toro A (2021) Low-cost smartphone-controlled potentiostat based on Arduino for teaching electrochemistry fundamentals and applications. Heliyon 7:e06259. https://doi.org/10.1016/j.heliyon.2021.e06259
11. Demirhan A, Eksin E, Kilic Y, Erdem A (2022) Low-Cost High-Resolution Potentiostat for Electrochemical Detection of Nucleic Acids and Biomolecular Interactions. Micromachines (Basel) 13:1610. https://doi.org/10.3390/mi13101610
12. Meloni GN (2016) Building a microcontroller based potentiostat: A inexpensive and versatile platform for teaching electrochemistry and instrumentation. J Chem Educ 93:1320–1322. https://doi.org/10.1021/acs.jchemed.5b00961
13. Ning ZH, Huang JQ, Guo SX, Wang LH (2020) A Portable Potentiostat for Three-Electrode Electrochemical Sensor. J Phys Conf Ser 1550:042049. https://doi.org/10.1088/1742-6596/1550/4/042049

14. Anshori I, Ramadhan IF, Ariasena E, et al (2022) ESPotensio: A Low-Cost and Portable Potentiostat with Multi-Channel and Multi-Analysis Electrochemical Measurements. IEEE Access 10:112578–112593. https://doi.org/10.1109/ACCESS.2022.3213725
15. David R, Duke J, Jain A, et al (2021) TensorFlow Lite Micro: Embedded Machine Learning on TinyML Systems. In: Proceedings of Machine Learning and Systems (MLSys). pp 800–811
16. Warden P, Situnayake D (2019) TinyML: Machine Learning with TensorFlow Lite on Arduino and Ultra-Low-Power Microcontrollers. O'Reilly Media, Sebastopol, CA, USA
17. Kang M, Kim D, Kim J, et al (2024) Strategies to Enrich Electrochemical Sensing Data with Analytical Relevance for Machine Learning Applications: A Focused Review. Sensors 24:3855. https://doi.org/10.3390/s24123855
18. World Health Organization Lead poisoning (fact sheet). https://www.who.int/news-room/fact-sheets/detail/lead-poisoning-and-health. Accessed 14 Aug 2026
19. U.S. Food and Drug Administration (2010) Questions and Answers on Lead-Glazed Traditional Pottery. https://www.fda.gov/food/environmental-contaminants-food/questions-and-answers-lead-glazed-traditional-pottery. Accessed 14 Aug 2026
20. Larsen B, Sánchez-Triana E (2023) Global health burden and cost of lead exposure in children and adults: a health impact and economic modelling analysis. Lancet Planet Health 7:e831–e840. https://doi.org/10.1016/S2542-5196(23)00166-3
21. (1984) Council Directive 84/500/EEC of 15 October 1984 on the approximation of the laws of the Member States relating to ceramic articles intended to come into contact with foodstuffs. Official Journal of the European Communities
22. International Organization for Standardization (2019) ISO 6486-1:2019 — Ceramic ware, glass ceramic ware and glass dinnerware in contact with food — Release of lead and cadmium — Part 1: Test method
23. ASTM International (2016) ASTM C738-94(2016): Standard Test Method for Lead and Cadmium Extracted from Glazed Ceramic Surfaces
24. U.S. Food and Drug Administration (2005) Compliance Policy Guide Sec. 545.450: Pottery (Ceramics); Import and Domestic — Lead Contamination. Silver Spring, MD, USA
25. Borrill AJ, Reily NE, Macpherson J V. (2019) Addressing the practicalities of anodic stripping voltammetry for heavy metal detection: A tutorial review. Analyst 144:6834–6849. https://doi.org/10.1039/C9AN01437C
26. Barton J, García MBG, Santos DH, et al (2016) Screen-printed electrodes for environmental monitoring of heavy metal ions: a review. Microchimica Acta 183:503–517. https://doi.org/10.1007/s00604-015-1651-0
27. Ndoye M, Kane C, Gadji EMR, et al (2018) Determination of Lead in Water by Linear Sweep Anodic Stripping Voltammetry (LSASV) at Unmodified Carbon Paste Electrode: Optimization of Operating Parameters. Am J Analyt Chem 9:171–186. https://doi.org/10.4236/AJAC.2018.93015
28. Mandil A, Amine A (2009) Screen-Printed Electrodes Modified by Bismuth Film for the Determination of Released Lead in Moroccan Ceramics. Anal Lett 42:1245–1257. https://doi.org/10.1080/00032710902901772

29. Baranwal AR, Dudala S, Rewatkar P, et al (2021) Development of Completely Automated Poly Potential Portable Potentiostat. ECS Journal of Solid State Science and Technology 10:027001. https://doi.org/10.1149/2162-8777/abdc15
30. Bard AJ., Faulkner LR. (2001) Electrochemical methods : fundamentals and applications. John Wiley & Sons, Inc.
31. International Council for Harmonisation (2023) ICH Q2(R2): Validation of Analytical Procedures. ICH, Geneva
32. Sheets RW (1997) Extraction of lead, cadmium and zinc from overglaze decorations on ceramic dinnerware by acidic and basic food substances. Sci Total Environ 197:167–175. https://doi.org/10.1016/S0048-9697(97)05431-4
33. Szynal T, Rebeniak M, Mania M (2016) Migration studies of nickel and chromium from ceramic and glass tableware into food simulants. Rocz Panstw Zakl Hig 67:247–252
34. Ainla A, Mousavi MPS, Tsaloglou MN, et al (2018) Open-Source Potentiostat for Wireless Electrochemical Detection with Smartphones. Anal Chem 90:6240–6246. https://doi.org/10.1021/acs.analchem.8b00850
35. Lopin P, Lopin K V. (2018) PSoC-Stat: A single chip open source potentiostat based on a Programmable System on a Chip. PLoS One 13:e0201353. https://doi.org/10.1371/journal.pone.0201353
36. Brown EW, Glasscott MW, Conley K, et al (2022) ACEstat: A DIY Guide to Unlocking the Potential of Integrated Circuit Potentiostats for Open-Source Electrochemical Analysis. Anal Chem 94:4906–4912. https://doi.org/10.1021/ACS.ANALCHEM.1C04226
37. Matsubara Y (2021) A Small yet Complete Framework for a Potentiostat, Galvanostat, and Electrochemical Impedance Spectrometer. J Chem Educ 98:3362–3370. https://doi.org/10.1021/acs.jchemed.1c00228
38. Jenkins DM, Lee BE, Jun S, et al (2019) ABE-Stat, a Fully Open-Source and Versatile Wireless Potentiostat Project Including Electrochemical Impedance Spectroscopy. J Electrochem Soc 166:B3056–B3065. https://doi.org/10.1149/2.0061909jes
39. Dobbelaere T, Vereecken PM, Detavernier C (2017) A USB-controlled potentiostat/galvanostat for thin-film battery characterization. HardwareX 2:34–49. https://doi.org/10.1016/j.ohx.2017.08.001
40. Zhao G, Tran TT, Modha S, et al (2022) Multiplexed Anodic Stripping Voltammetry Detection of Heavy Metals in Water Using Nanocomposites Modified Screen-Printed Electrodes Integrated With a 3D-Printed Flow Cell. Front Chem 10:815805. https://doi.org/10.3389/fchem.2022.815805
41. von Zuben TW, Salles AG, Bonacin JA (2024) Low-cost open-source potentiostats: A comprehensive review of DIY solutions and fundamental concepts of electronics and its integration with electrochemistry. Electrochim Acta 498:144619. https://doi.org/10.1016/j.electacta.2024.144619